# Effects of a Trapped Vortex Cell on a Thick Wing Airfoil

**Davide Lasagna** · **Raffaele Donelli** · **Fabrizio De Gregorio** · **Gaetano Iuso**

**Abstract** The effects of a Trapped Vortex Cell (TVC) on the aerodynamic performance of a NACA0024 wing model were investigated experimentally at $Re = 10^6$ and $6.67 \cdot 10^5$. The static pressure distributions around the model and the wake velocity profiles were measured to obtain lift and drag coefficients, for both the clean airfoil and the controlled configurations. Suction was applied in the cavity region to stabilize the trapped vortex. For comparison, a classical boundary layer suction configuration was also tested. The drag coefficient curve of the TVC controlled airfoil showed sharp discontinuities and bifurcative behaviour, generating two drag modes. A strong influence of the angle of attack, the suction rate and the Reynolds number on the drag coefficient was observed. With respect to the clean airfoil, the control led to a drag reduction only if the suction was high enough. Compared to the classical boundary layer suction configuration, the drag reduction was higher for the same amount of suction only in a specific range of incidence, i.e. $\alpha = -2°$ to $\alpha = 6°$ and only for the higher Reynolds number. For all the other conditions, the classical boundary layer suction configuration gave better drag performances. Moderate increments of lift were observed for the TVC controlled airfoil at low incidence, while a 20% lift enhancement was observed in the stall region with respect to the baseline. However, the same lift increments were also observed for the classical boundary layer suction configuration. Pressure fluctuation measurements in the cavity region suggested a very complex interaction of several flow features. The two drag modes were characterized by typical unsteady phenomena observed in rectangular cavity flows, namely the shear layer mode and the wake mode.

Gaetano Iuso, Davide Lasagna
Politecnico di Torino, Dipartimento di Ingegneria Aeronautica e Spaziale, Corso Duca degli Abruzzi, 24, 10129 Torino, Italy
E-mail: gaetano.iuso@polito.it
Raffaele Donelli, Fabrizio De Gregorio
C.I.R.A., Centro Italiano di Ricerca Aerospaziale

## 1 Introduction

Advanced flow control techniques are nowadays required in order to improve the performances of modern aircraft. An interesting but not greatly investigated flow control strategy is the so-called "trapped vortex cell" control, from hereon referred to as TVC. This technique requires a properly shaped cavity positioned along the spanwise direction on the upper surface of the airfoil. Under certain flow conditions, a steady, large vortical structure forms in the cavity creating a recirculating region closed by the dividing streamline. The idea of trapping a vortex is not new as it was first mentioned by Ringleb (1961). Following this work, several applications of the trapped vortex concept for flow control have been studied. Adkins (1975) demonstrated experimentally that the pressure recovery in a short diffuser could be strongly enhanced by a stabilized trapped vortex. There are also two known examples of flight testing, namely the Kasper wing, (see Kasper (1974)) and the EKIP aircraft, (see Savitsky et al (1995)).

More recently, several investigations, theoretical, numerical and experimental, have been carried out in the framework of the EU project VortexCell2050. Savelsberg and Castro (2008) studied experimentally the flow inside a large aspect ratio cylindrical cell. In this case, the flow in the cavity, driven by the shear layer forming in the opening, showed a nearly solid body rotation although the mean velocity profile was significantly distorted into an S shape due to three dimensional effects. This spanwise modulation of the transversal velocity was also observed in a large eddy simulation performed by Hokpunna and Manhart (2007). Donelli et al (2009) simulated the vortex cell flow as purely two dimensional and presented a comparison between several approaches. The authors concluded that the Prandtl-Batchelor model produces similar results to RANS simulations, which in turn compare favourably to experimental results. Iollo and Zannetti (2001) have shown that a trapped vortex can have a limited stability

region. The authors demonstrated that, under certain conditions, the vortex is unstable and cannot be kept trapped if some control in the cavity region is not exerted. For this reason different control strategies have been proposed and tested. De Gregorio and Fraioli (2008) have demonstrated experimentally, by means of PIV measurements on a cavity located on an airfoil, that a coherent vortex formed only if suction was applied in the cavity region.

Most of the work on cavity flows has focused on simpler geometries, e.g. rectangular cavities. Although this is not a suitable shape for trapping a vortex on a wing, the fundamental flow mechanisms observed in such a configuration are still important for a flow control application. Rockwell and Naudascher (1979) provide a comprehensive review of the subject. Maull and East (1963); Rockwell and Knisely (1980); Faure et al (2009); Migeon (2002); Larchevêque et al (2007) have investigated the flow complexity in rectangular cavities highlighting a three dimensional organization of the flow. Brès and Colonius (2008) investigated rectangular cavity flows through direct numerical simulations. The authors evidenced the presence of complex three-dimensional global instabilities with a spanwise wavelength nearly equal to the cavity depth that oscillate at a much lower value than the two-dimensional Rossiter instabilities. Moreover, the three-dimensional instabilities were strictly related to the centrifugal instability mechanism.

Cavity flows are also characterized by self-sustained oscillations, occurring in a broad range of incoming flow parameters and cavity geometries, as shown by Rowley et al (2001). Two main types of oscillations have been observed: the shear-layer mode and the wake mode. The shear-layer mode, associated with the spatial instability of the vorticity layer bounding the cavity, is usually described in terms of the acoustic feedback process introduced by Rossiter (1964). It is characterized by a Strouhal number $St = fL/U_e$, based on the cavity length $L$ and on the free-stream velocity $U_e$, of the order of unity, according to the Mach number. The wake mode oscillation, observed experimentally by Gharib and Roshko (1987) and in numerical simulations by Rowley et al (2001) and Suponistsky et al (2005), is dominated by a low frequency large scale vortex shedding, similar to the shedding of vortices in the wake of bluff bodies. Such a regime is associated with large amplitude fluctuations and with an increase of the cavity drag. It is characterized by a Strouhal number of the order of 0.07.

Other studies have focused their attention on the effects of d-type roughness on the structure of a flat plate turbulent boundary layer, in order to obtain skin friction drag reduction. d-type roughness, which consists of sparsely spaced two dimensional square grooves whose size is much lower than the boundary layer, has been experimentally demonstrated to reduce the turbulent skin friction drag by Choi and Fujisawa (1993). The authors found that the near wall structure of the turbulent boundary layer was modified by a vortex in the cavity, which absorbed and reorganized the incoming near wall turbulence downstream of the cavity.

The TVC flow control technique lacks the support of experimental data regarding its effectiveness in controlling the flow over a wing profile. Olsman and Colonius (2011) recently published a paper on this subject, although the Reynolds number of their experiment was almost two orders of magnitude lower than that of the present experiment and no control was operated in the cavity. Using two dimensional direct numerical simulations and dye flow visualizations, the authors studied the complex flow physics arising from the interaction of the cavity flow with the external flow. The interaction developed into several cavity flow regimes. According to the angle of attack, the authors highlighted the first and the second shear layer mode. These oscillations generated vortices which delayed separation. Moreover, at specific incidences the authors suggested the possibility of a higher lift to drag ratio for the airfoil with the cavity.

In the present paper the experimental results obtained in the wind tunnel investigation performed on a wing equipped with a trapped vortex cavity are reported. The main objective of the investigation was to assess the effects of the TVC flow control technique on the aerodynamic performance of the airfoil and to compare it with a conventional boundary layer suction system. The experiments also focused on investigating the complex unsteady phenomena taking place in the cavity trapping the vortex. The paper is organized as follows: the lift and drag characteristics of the controlled configuration are shown and compared with the clean airfoil configuration and with the classical boundary layer suction configuration. Some selected static pressure distributions and wake velocity profiles are then shown and discussed. Finally, results of the analysis of the unsteady pressure measurements taken inside and outside the cavity region are discussed, to give some insight into the unsteady flow dynamics taking place.

## 2 Experimental setup and data reduction

### 2.1 Model and test section configuration

A closed-circuit wind tunnel, with test section diameter and length equal to 3 m and 5 m, respectively, was used in this investigation. Maximum velocity and turbulence level in this facility are equal to 90 m/s and 0.4%, respectively. The experiments were conducted on a wing with a chord length of 0.5 m and a span of 1.2 m, with a NACA0024 section. Tests were performed at Reynolds numbers based on the airfoil's chord equal to $10^6$ and $6.67 \cdot 10^5$.

The central upper part of the model could be replaced with different modules, so different configurations were tested, namely the baseline, (B), the baseline with classical boundary
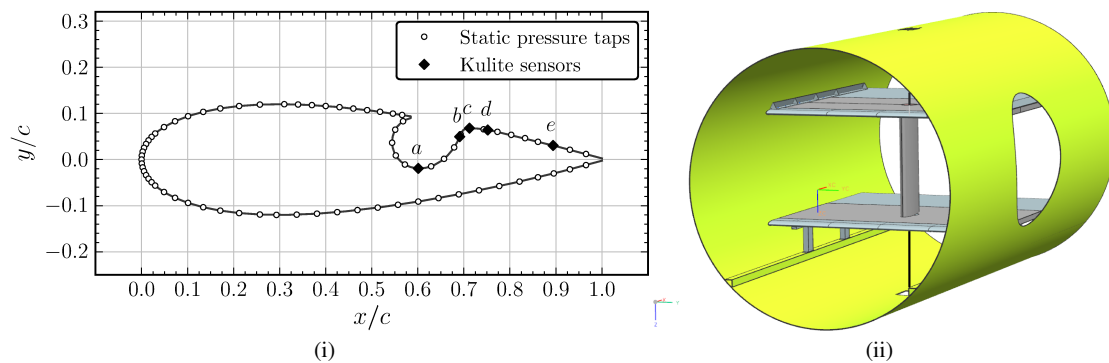
**Fig. 1** (i) - Geometry of the NACA0024 wing section with the vortex cell. The locations of the Kulite sensors and of the static pressure taps for the TVC/TVCS configurations are also shown. (ii) - Sketch of the wind tunnel test section arranged for the experiment.

layer suction (BS), and the trapped vortex cavity with/without suction (TVCS/TVC). These modules extended along the chord from $x/c = 0.30$ to $x/c = 0.84$.

The TVC module housed a cavity previously designed by Chernyshenko et al (2008) with a Prandtl-Batchelor flow model. The cavity extended from $x/c \approx 0.58$ to $x/c \approx 0.71$ with an opening length $L = 60$ mm and a span $b = 400$ mm, resulting in an aspect ratio $b/L = 6.66$.

Suction was operated through the upstream portion of the cavity surface. The perforated wall occupied 39 mm along the cavity surface and 390 mm in the spanwise direction. 2246 holes with a diameter of 1 mm were drilled in this region, resulting in a porosity of 11.6%. In figure 1(i) the geometry of the airfoil with the vortex cell is shown.

The BS configuration module replicated the geometry of the NACA 0024 airfoil but presented a porous region between $x/c = 0.59$ and $x/c = 0.66$. The porous surface consisted of 1980 holes of 1 mm diameter and extended 384 mm in the spanwise direction, with a porosity equal to about 10%.

The model was fixed vertically in the test section by two hollow shafts, the lower one being connected to a motorized rotation system to change the model's incidence. It was placed between two 60 mm thick rectangular aluminium honeycomb panels fitted horizontally at the model's tips, spanning the entire width, as shown in figure 1(ii). The panels extended in the streamwise direction from one chord upstream of the model's leading edge to three chords downstream the trailing edge.

A suction pump located outside the test section, which provided up to 80 m$^3$/h of volumetric flow rate, was connected to a plenum chamber inside the model, just behind the perforated walls of the TVCS and BS modules. The suction rate was measured by a SD8000 flow meter from IFM Electronics and was set by means a bleed valve located between the flow meter and the pump.

## 2.2 Instrumentation, data acquisition and data reduction

Pressure distributions on the model's surface were measured by 71/81 static pressure taps, depending on the module mounted, in the mid span section of the model, located as shown in figure 1(i) for the TVC/TVCS configurations. Six pressure taps were located in the cavity bottom, at $x/c = 0.6$, along the spanwise direction. Differential pressure measurements were performed using two 64-channel ZOC33 Scanivalve pressure transducers. The full scale of the transducers was equal to $\pm 10$ inH$_2$O for 112 channels and $\pm 20$ inH$_2$O for the remaining ones. The transducers had an accuracy of 0.15% of the full scale value.

The wake investigations were performed with a wake rake located two chords downstream of the model's trailing edge, positioned in the centre of the test section corresponding to the mid span of the cavity. It was equipped with 44 total pressure probes and 3 static pressure probes, to take into account the static pressure recovery in the wake for the drag coefficient calculation. The static pressure probes were calibrated to consider the influence of the wake rake body. A traverse system allowed the wake rake to be positioned with respect to the model's wake. All the pressure probes were connected to three DSA3217 Scanivalve systems, each with 16 channel inputs. The full scale value was equal to $\pm 10$ inH$_2$O, and the transducers accuracy was 0.2% of the full scale value. The pressure signals around the model and in the wake were sampled at $f = 0.5$ Hz for three minutes.

For the TVC/TVCS configurations, pressure fluctuation measurements in the cavity region and downstream of it were performed in the mid span section with five XCS-093 Kulite pressure transducers. The external diameter of these transducers was equal to 2 mm, they were thermally compensated and they had a full scale value equal to $\pm 5$ psi. The location of these transducers is shown in figure 1(i).

The output signals from the five Kulite sensors and from the flow meter were simultaneously sampled by a National Instruments CDAQ system with NI 9239 modules with 4

input channels each, with an A/D converter resolution equal to 24 bits. The acquisition system was equipped with an anti-aliasing filter with cut-off frequency equal to $0.46 \cdot f_{sampling}$. The pressure signals were collected at a sampling frequency of 8 KHz and $2^{20}$ pressure samples were acquired, providing a sufficient convergence of the statistics.

The lift coefficient was evaluated by integrating the pressure distribution on the model. The drag coefficient was estimated by momentum balance, using the total and static pressure distributions from the wake rake measurements using Jones' formula, (Schlichting, 1954).

Because of the blockage effects produced by the rig in the test section, static, dynamic and total pressure correlations were taken between the Pitot ring at the exit of the contraction section and the test section.

Wind tunnel wall corrections, namely lift interference, solid and wake blockage, were taken into account as described in AGARD-AR-336 (1998). The corrections were less than 5% over all the range of incidences tested. The accuracy of the aerodynamic coefficients was also evaluated as outlined in AGARD-AR-304 (1994). The lift coefficient absolute uncertainty was less than 0.01, while for the drag coefficient this value was less than 0.0001.

In the following discussion, the non dimensional volumetric suction rate $S = Q/(bcU_\infty)$ will be used, where $Q$ is the dimensional volumetric flow rate, $b$ is the cavity span, $c$ is the chord and $U_\infty$ is the reference air speed.

## 3 Results

### 3.1 Lift and drag curves

Lift coefficient curves are reported in figure 2, for $Re = 10^6$. The curves refers to the four configurations tested, namely the baseline (B), the baseline with suction (BS), the trapped vortex cell with suction (TVCS) and without suction (TVC). For the two configurations with suction, BS and TVCS, the suction parameter $S$ is equal to 0.0037, which corresponds to the maximum value available in the experiments. The figure also include the results of some of the repeatability tests performed, reported with closed symbols.

It can be observed that TVCS gives a larger lift than the baseline case. The benefits, while more substantial in the stall region, are minor at low incidence. In fact, the maximum lift coefficient $C_{L_{max}}$ increases from 0.96 (B) to 1.15 (TVCS), that is by 20%. Furthermore, for the TVCS case the stall occurs at an angle of attack $\alpha = 19°$, while the clean airfoil stalls at $\alpha = 16°$. If no suction is applied, i.e. TVC case, the performances are practically equal to that of the baseline, if not worse at large incidences.

Most importantly, the TVCS configuration gives a lift coefficient not greater than the classical boundary layer suction configuration for the same amount of suction.

Figure 3 shows the results of the drag coefficient for the same cases and conditions in figure 2. Note that for clarity the $C_D$ scale is logarithmic. The drag curve of the TVC configuration shows that, without suction, the presence of the trapped vortex cell results in an increase of the drag with respect to the baseline configuration, over the whole range of incidence. On the other hand, if suction is applied, i.e. the TVCS case, the drag coefficient decreases, by an amount which depends on the angle of attack. However, complex behaviour characterizes the drag curve of the TVCS configuration. In fact, two different branches are observed, which separate at an angle of attack equal to $2°$ and converge at $\alpha \approx 12°$. In the following discussion these two branches will be referred to as the low (LD) and high (HD) drag modes. At $\alpha = 2°$ the two branches give a very different drag coefficient value: 0.0051 for the LD branch and 0.0081 for the HD branch. At $\alpha = -2°$ another step in the drag curve is observed, where the drag coefficient changes from 0.0096 to 0.0071. As will be shown later these steps are related to a reorganization of the cavity flow, which occurs when the incidence reaches a critical value, for a given suction rate.

It has to be noted that the two drag modes of the TVCS configuration were obtained from different experimental procedures, even though the flow conditions were nominally the same, i.e. $S = 0.0037$ and $Re = 10^6$. The HD case, (curve "TVCS; S=0.0037", figure 3 ), was obtained performing the measurements so that the suction pump was switched off and then on for each angle of attack. This procedure caused the drag coefficient to increase from $\alpha = 2°$ to $\alpha = 4°$. For the LD case, (curve "TVCS; S=0.0037; Rep. Tests 1"), obtained in a subsequent experiment, the tests were conducted by increasing the angle of attack while keeping the value of the suction parameter constant.

We also performed further experiments, (curve "TVCS; S=0.0035; Rep. Tests 3", figure 3), following the second procedure but with a slightly lower suction rate, $S = 0.0035$. For these tests the drag coefficient suddenly increased again at $\alpha = 2°$, from the LD mode to the HD mode.

Such behaviour seems to indicate that, at a given incidence, a particular drag mode can take place depending on the history of the flow and on the value of the suction rate.

The BS configuration shows continuous behaviour and as expected gives a drag coefficient lower than the baseline over all the range of angles of attack. It appears that for the same amount of suction, $S = 0.0037$, there is a range of incidences where the TVCS configuration gives a lower drag coefficient than the classical boundary layer suction configuration, if the LD branch is considered. This range covers the low-mid incidences, i.e. $-2° \leqslant \alpha \leqslant 8°$. On the other hand, outside this range, the classical boundary layer suction system is more effective in reducing the drag of the airfoil, especially at high incidences.
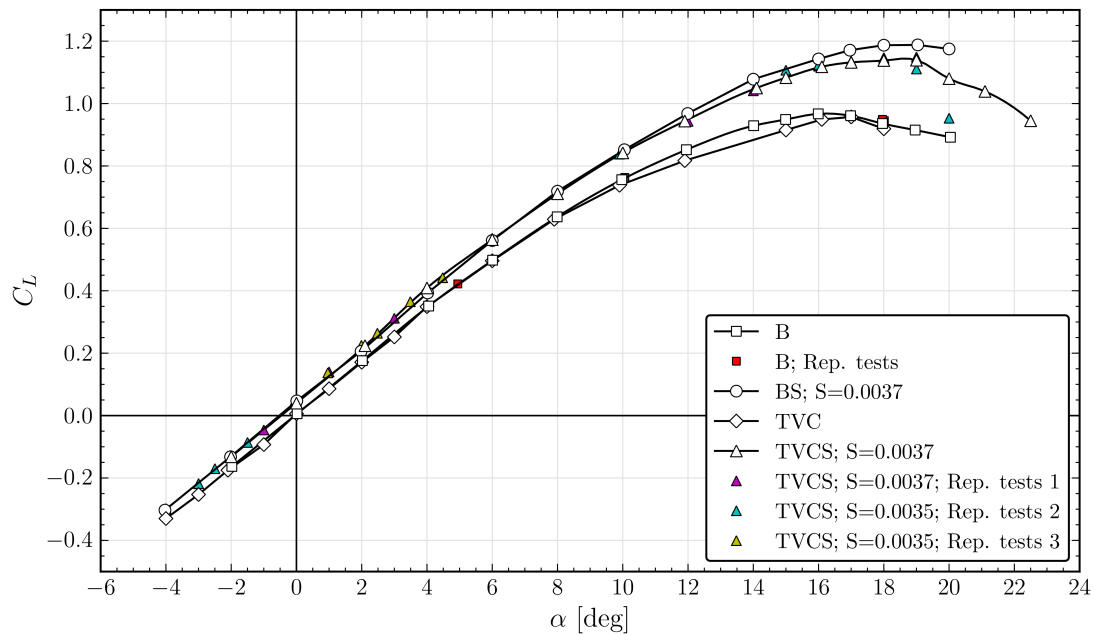
**Fig. 2** Lift coefficient curves for the Baseline (□), the Baseline with suction (○), the TVC (◇), and the TVCS (△) configurations. Repeatability tests are also shown in closed symbols. $Re = 10^6$.
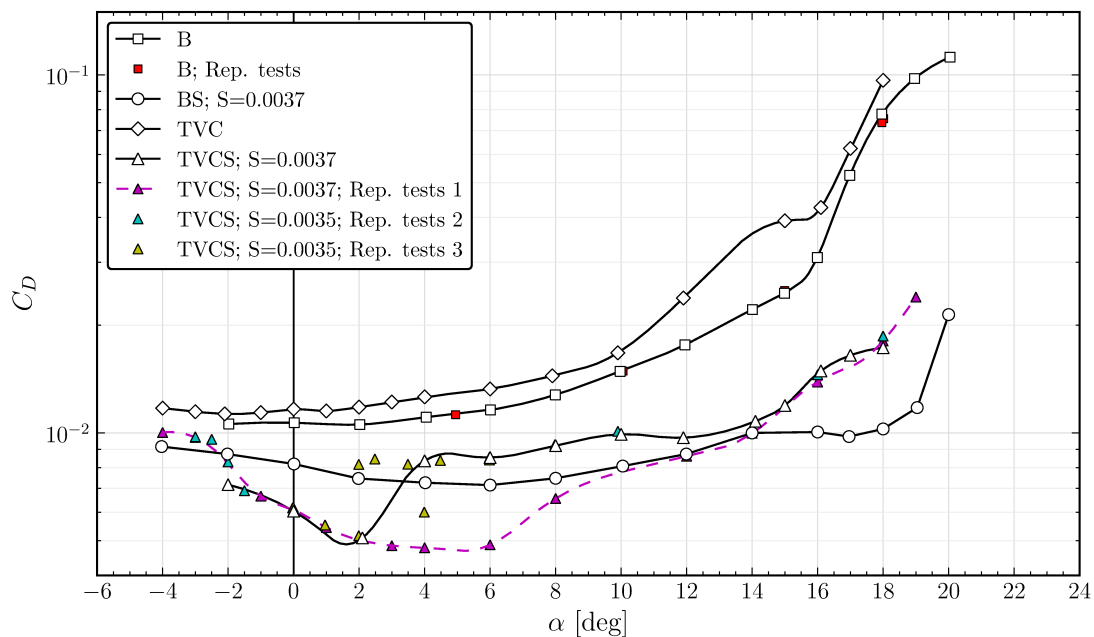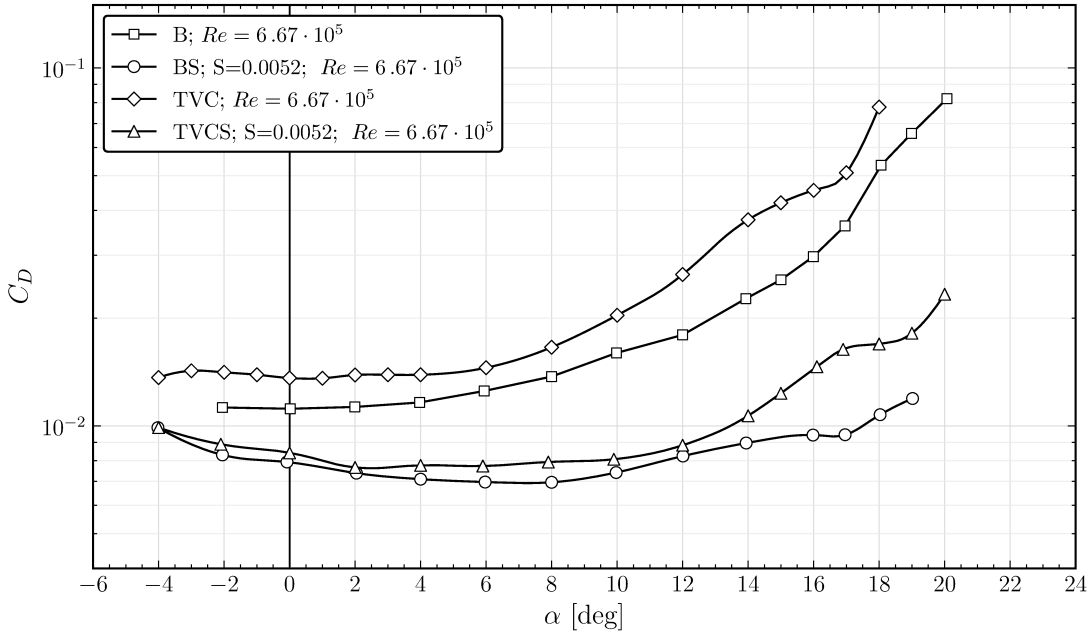


**Fig. 3** Drag coefficient curves for the Baseline (□), the Baseline with suction (○), the TVC (◇), and the TVCS (△) configurations. Repeatability tests are also shown in closed symbols. $Re = 10^6$.

To summarize, the main aerodynamic characteristics are reported for the four configurations in table 1, for $Re = 10^6$. Interestingly, the TVCS configuration reaches the maximum lift to drag ratio at an angle of attack, $\alpha = 6°$, for the LD case. On the contrary, the BS configuration evidences a maximum lift to drag ratio in the stall region, for $\alpha = 17°$, where the classical boundary layer suction is more effective compared to the trapped vortex cell in delaying flow separation.

It has to be noted that despite the fact that the lift curves of the BS and the TVCS$_{LD/HD}$ configuration are practically superimposed, the drag curves behave differently. From this point of view it can be argued that several mechanisms are involved in the lift and drag generation of the airfoil in the three configuration. Later in the paper these aspects will be discussed more in detail.

Figure 4 shows the drag coefficient curves for $Re = 6.67 \cdot 10^5$, for the four configurations presented above. The

**Fig. 4** Drag coefficient curves for the Baseline (□), the Baseline with suction (○), the TVC (◇), and the TVCS (△) configurations. $Re = 6.67 \cdot 10^5$.

| Configuration | $C_{D_{min}}$ | $C_{D_0}$ | $C_{L_{max}}$ | $\alpha_{st}$ | $(C_L/C_D)_{max}$ | $\alpha_{(C_L/C_D)_{max}}$ |
|---|---|---|---|---|---|---|
| B | 0.0105 | 0.0106 | 0.967 | 16° | 51 | 10° |
| BS | 0.0072 | 0.0083 | 1.183 | 19° | 113 | 17° |
| TVC | 0.0113 | 0.0116 | 0.957 | 17° | 44 | 10° |
| TVCS$_{LD}$ | 0.0048 | 0.0061 | 1.149 | 19° | 116 | 6° |

**Table 1** Summary of the aerodynamic performance of the four configurations for $Re = 10^6$.

suction parameter $S$ at the lower Reynolds number is equal to 0.0052, that is 50% higher than at $Re = 10^6$, because of the lower free-stream velocity. As witnessed for the higher Reynolds number, without suction the presence of the cell on the airfoil implies a larger drag with respect to the baseline. Furthermore, for the lower Reynolds number, only one drag curve was observed for the TVCS configuration, which gave a lower drag coefficient than the clean airfoil. As will be discussed later in the paper, this curve corresponds to an HD mode. However, at the lower Reynolds number the classical boundary layer suction always results in a lower drag coefficient compared to the trapped vortex cell configuration, for the same amount of suction, over the whole range of angles of attack.

Regarding the lift coefficient curves for $Re = 6.67 \cdot 10^5$, not reported here for brevity, similar results to $Re = 10^6$ were obtained. In fact, the lift curves of the BS and TVCS configuration were practically equal over the whole range of angles of attack, except in the stall region, where the classical boundary layer suction system gave slightly higher lift coefficients compared to the TVCS.

This last result clearly evidences the complexity of the cavity flow and of the effectiveness of the TVC control, which also depends on the Reynolds number.

### 3.2 Pressure distributions and wake velocity profiles

As an example of the results, selected pressure distributions and wake velocity profiles are reported for $\alpha = 6°$ and $\alpha = 18°$, which are representative of fully attached and separated flow conditions. Results are presented only for $Re = 10^6$.

In figure 5 pressure distributions are shown for $\alpha = 6°$, for the clean and the TVCS configurations, (HD mode). The pressure distribution inside the cavity is quite complex. There is a stagnation point on the downstream cavity edge at $x/c \approx 0.72$, where the cavity shear layer impinges, followed upstream by a short region of strong negative pressure gradient. There then follows a region of adverse pressure gradient up to $x/c \approx 0.55$. Outside the cavity the pressure distribution of the TVCS configuration is characterized by a slightly larger pressure difference between the upper and the lower surfaces, corresponding to the slightly larger lift coefficient observed in figure 2. This is probably due mainly to the suction, since similar characteristics are observed also for the BS configuration, not reported here in the figure for clarity. Furthermore, in the trailing edge region, the TVCS configuration shows a better pressure recovery.
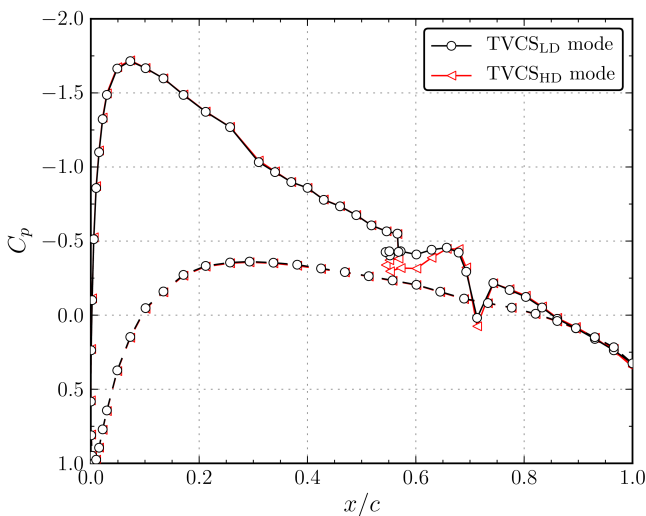
In figure 6 the static pressure distributions for the two drag modes are reported for $\alpha = 6°$, at which the differ-
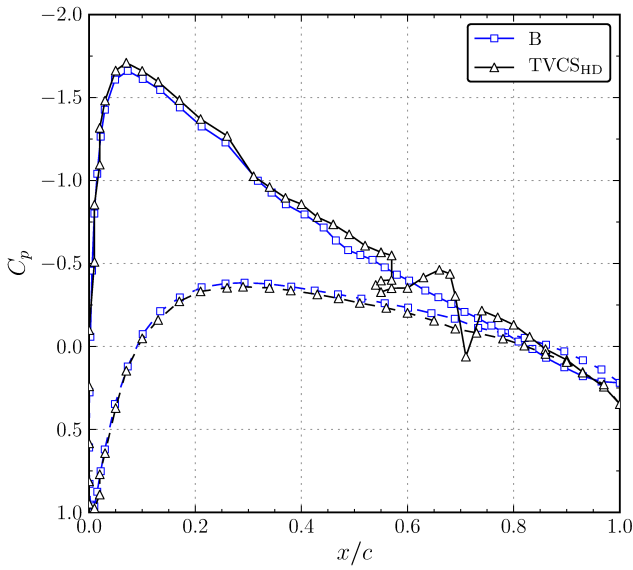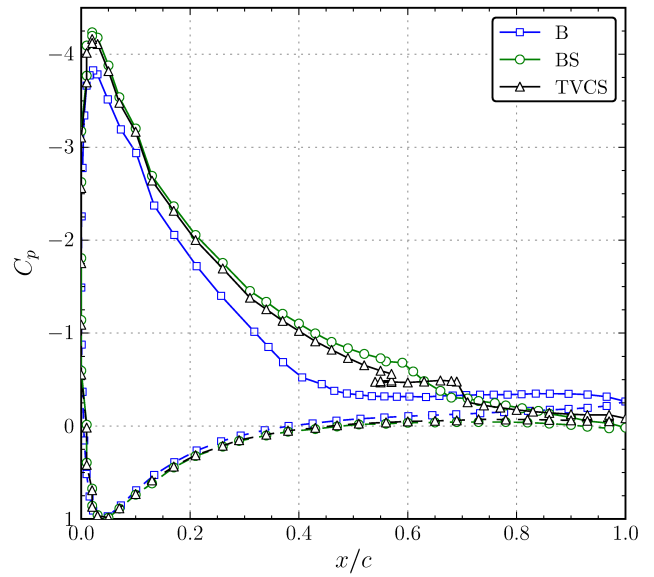
**Fig. 5** Static pressure coefficient distributions for the Baseline (□) and for the TVCS$_{HD}$ (△) configurations; $\alpha = 6°$. Broken curves refers to the airfoil's lower surface.

**Fig. 7** Static pressure coefficient distributions for the Baseline (□), the Baseline with classical boundary layer suction (○) and for the TVCS (△) configurations;; $\alpha = 18°$. Broken curves refers to the airfoil's lower surface.

ences between the two modes are largest. It appears that the pressure distributions are almost superimposed and the only difference occurs inside the cavity. More precisely, the adverse pressure gradient inside the cavity appears less severe for the LD mode. Interestingly, this slight difference is responsible for a large variation of the drag coefficient, which gives a clear indication that the cavity flow is crucial for the effectiveness of the trapped vortex cell in controlling the external flow. In section 3.4 an physical interpretation of the two drag modes will be given.
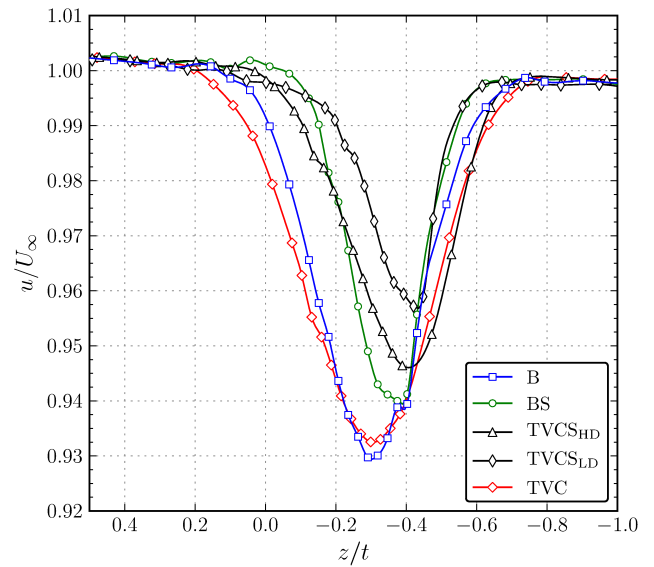
For $\alpha = 18°$, figure 7, the pressure distribution in the cavity for the TVCS configuration is almost constant, probably because of the flow separation occurring at the cavity's cusp.

**Fig. 8** Non dimensional wake velocity profiles for the Baseline (□), the Baseline with classical boundary layer suction (○), the TVCS$_{HD}$ (△), the TVCS$_{LD}$ (◇), and the TVC (◇) configurations. $\alpha = 6°$.

**Fig. 6** Pressure coefficient distributions or the LD (◁) and HD (○) modes. $\alpha = 6°$.

Nevertheless the pressure distribution is modified compared to the clean configuration, especially upstream of the cavity, where a lower pressure characterizes the TVCS configuration. While the clean airfoil exhibits separation at 45% of the chord, the TVCS moves downstream the separation point, in correspondence of the cusp, with a weak pressure recovery up to the trailing edge. Similar characteristics are evidenced by the BS configuration, which also shows a strong pressure recovery in the porous region, from $x/c = 0.59$ to $x/c = 0.66$.
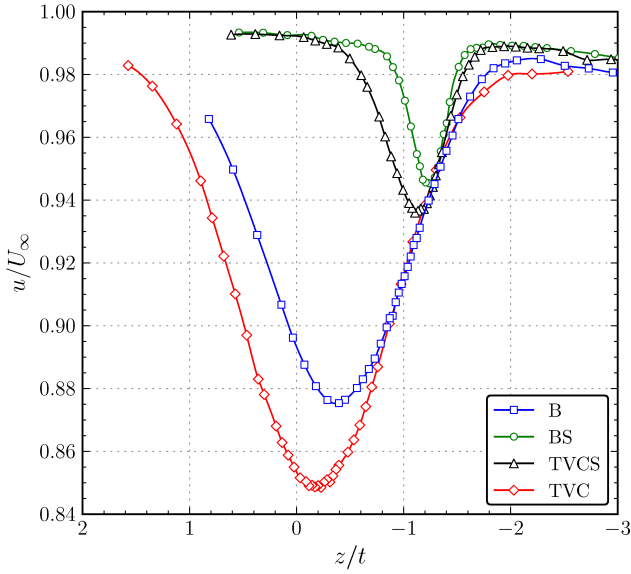
**Fig. 9** Non dimensional wake velocity profiles for the Baseline (□), the Baseline with classical boundary layer suction (○), the TVCS (△) and the TVC (◇) configurations. $\alpha = 18°$.



**Fig. 10** Spanwise pressure coefficient distributions along the cavity bottom wall, $x/c = 0.6$. (a) LD mode; (b) HD mode. $\alpha = 2°, 4°, 6°, 8°$. $S = 0.0037$.

It is probable that the better pressure recovery of the TVCS is in part due to the effect of the suction in the cavity.

Wake velocity profiles for $\alpha = 6°$ and $\alpha = 18°$ are reported in figures 8 and 9, respectively. At the lower incidence it is clear that the wake of the TVCS$_{LD}$ configuration is narrower than that of the BS case and evidences a lower momentum deficit. On the other hand, the wake of the TVCS$_{HD}$ configuration is larger, although it shows a lower maximum velocity deficit. It also appears that the velocity distribution of the TVC is larger than that of the clean airfoil.

For $\alpha = 18°$ it appears that the wake of the BS configuration is narrower than that of the TVCS case. This indicates that, at large angles of attack, a classical boundary layer suction system is more effective in delaying flow separation that a trapped vortex cell control. It also appears that, without suction, the cell produces massive separation and gives a drag performance worse than that of the baseline.

Pressure distributions along the cavity span at $x/c = 0.6$, for both the LD and the HD modes, are reported in figure 10, for angles of attack equal to $2°, 4°, 6°$ and $8°$. Although just a few pressure taps were located along the cavity, it is evident that both drag modes present their own characteristic spanwise modulation of the pressure. The LD cases, figure 10(a), show an asymmetric spanwise pressure distribution with an amplitude equal to $\Delta C_p \approx 0.1 \div 0.15$, independent of $\alpha$ and translated to lower values as the angle of attack increases. The curve for $\alpha = 8°$ is significantly different from those of the lower incidences. This might indicate a modification of the flow organization after $\alpha = 6°$. Evidence of the effects of such reorganization is also found in the drag curve of figure 3, where the drag coefficient of the LD mode curve rises significantly after $\alpha = 6°$. Interestingly, the mirror
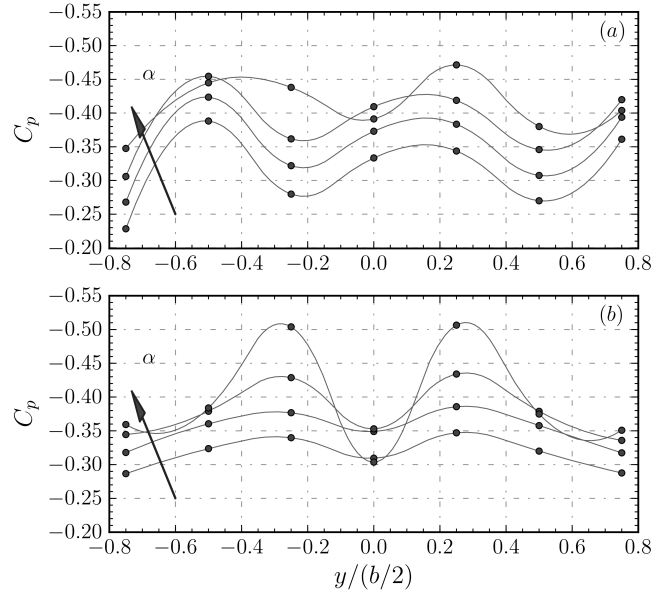
image of the asymmetric distribution was never observed, probably because of some geometrical imperfection of the setup which only triggered a particular configuration. On the other hand, the spanwise pressure distributions for the HD case, figure 10-b, show a symmetric modulation with an amplitude that grows with $\alpha$.

It is also evident that no matter what case is considered, the flow field has an intrinsic three-dimensional organization. The wavelength of the modulation of the pressure distributions can be roughly estimated to be $\lambda/b \approx 0.3$, or, in terms of cavity opening, $\lambda/L \approx 1.9$, for both modes.

A three-dimensional flow nature was also found for circular cavities by Savelsberg and Castro (2008) in terms of a modulation of the transversal velocity. The wavelength was about 2.15$L$. A three-dimensional organization has also been observed for high Reynolds number flows past rectangular cavities organized in a cell-like structure, for example by Maull and East (1963), with similar characteristics. Analogous three dimensional features were also highlighted by Brès and Colonius (2008) for a flow past a rectangular cavity at a lower Reynolds number.

### 3.3 Effects of the suction rate

The effects of the suction rate on the performance of the TVC controlled airfoil were tested at different angles of attack, namely $\alpha = 0°, 2°, 6°, 14°$ and $18°$, at $Re = 10^6$. The suction parameter was varied from the minimum value $S \approx 1.4 \cdot 10^{-3}$ up to $S \approx 3.7 \cdot 10^{-3}$. The results of the investigation are reported in figures 11 and 12 for the lift and drag coefficient, respectively.
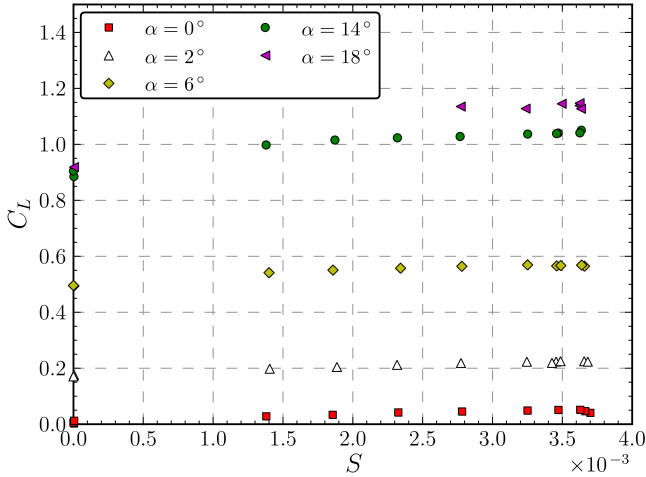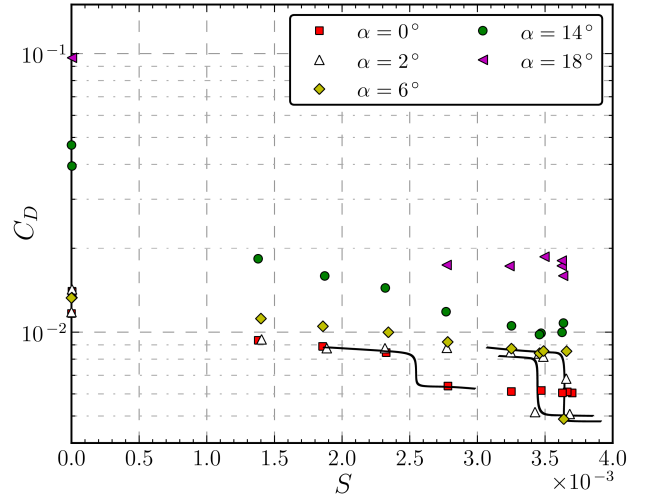
**Fig. 11** Effect of the suction parameter $S$ on the lift coefficient of the TVCS configuration, for several angles of attack. $Re = 10^6$.



**Fig. 12** Effect of the suction parameter $S$ on the drag coefficient of the TVCS configuration, for several angles of attack. $Re = 10^6$. The dark curves highlight the transition steps.

As the suction rate is increased the lift coefficient grows asymptotically, at all the angles of attack, and in particular at the higher incidences, where a high value of the suction strongly reduces the separation region. On the other hand, the drag coefficient is influenced much more by the suction rate and shows larger variations than the lift coefficient. It is noticeable that at all the angles of attack, the higher the suction rate, the smaller the drag coefficient. Only a minimum amount of suction, ($S = 1.4 \cdot 10^{-3}$), is sufficient to reduce the drag considerably, in particular at the higher incidences.

At low/mid incidences, a particular value of the suction parameter exists for which the drag coefficient suddenly falls. For $\alpha = 0°$ this critical value is somewhere around $S = 2.5 \cdot 10^{-3}$, while at a larger incidence, $\alpha = 2°$ and $\alpha = 6°$, approximate critical values are $S = 3.4 \cdot 10^{-3}$ and $S = 3.6 \cdot 10^{-3}$. Moreover, it can be observed that the height of the step increases as $\alpha$ increases. No critical values of the suction parameter were observed at $\alpha = 14°$ and $18°$, probably because these were higher than the maximum suction rate achievable in the experiments. As will be shown later, these transitions are related to a drastic reorganization of the cavity flow when the suction reaches a particular value. Similar behaviour was reported by Adkins (1975), who presented results concerning the effectiveness of a diffuser controlled by a trapped vortex stabilized by suction. In fact, the author observed a step of the diffuser static pressure recovery at particular values of the suction.

Interestingly, these steps are observed both in the drag curves of figure 3, as a consequence of the incidence variation, and in the curves of figure 12, where $S$ is the varying parameter.

## 3.4 Unsteady pressure analysis

An insight into the complexity of the flow interactions taking place in the cavity for the TVCS configuration for $Re = 10^6$ is given by the analysis of the pressure fluctuations measured by the Kulite sensors. In this section a summary of the results of this analysis is reported, in terms of energy spectra, autocorrelation and cross-correlation functions.

### 3.4.1 Spectral analysis

In figures 13(i) and 13(ii) the energy spectral density (ESD) of the pressure fluctuations are reported for locations **a** and **b**, respectively, (see figure 1 for sensor positions). All the spectra shown were obtained by averaging the FFT spectra of 50% overlapping blocks of $2^{16}$ points each, to reduce the uncertainty in the estimate. Furthermore, the blocks were tapered with a Hanning window, to reduce side-lobe leakage. Spectra corresponding to both HD and LD modes of the TVCS configuration are reported for several incidences, $-4° \leqslant \alpha \leqslant 12°$. The vertical scale has been artificially shifted by two decades for each curve after the first one to show all the spectra at different incidences. For the abscissa, the Strouhal number $St = fL/U_e$ was used, where $L = 60$ mm is the cavity opening length and $U_e$ is the external velocity, computed from the static pressure distributions. The spectra reveal several energy peaks, evidence of complex unsteady behaviour of the cavity flow. In figure 13(i), for $\alpha = -4°$ and $\alpha = -2.5°$, the spectra of sensor **a**, located at the bottom of the cavity, show a strong dominant peak centred at $St \approx 0.07$. This value is in good agreement with the Strouhal number associated with the wake mode, observed for rectangular cavities by several authors. This process, well described by Rowley et al (2001), consists in the periodic formation and ejection of

large scale vortices from the cavity, resulting from hydrodynamic instability. Gharib and Roshko (1987) associated this oscillation mode to a large cavity drag. Similar values of the Strouhal number were obtained for flows past a backward-facing step by the direct numerical simulations performed by Hung, Moin, and Kim (1997). These authors associated this value with the formation and detachment of large scale vortices from the step.

As the incidence increases to $\alpha = -2°$, the energy distribution changes drastically. The peak at $St = 0.07$ vanishes and a weaker peak for $S_t \approx 0.11$ appears. This modification of

the energy distribution can be associated with a change in the flow organization in the cavity, which in turn is likely associated to the drastic drag reduction observed in the drag curve of the TVCS configuration reported in figure 3 at $\alpha = -2°$. The energy distribution remains nearly the same up to $\alpha = 8°$ if the LD mode is considered, (black curves), even though the frequency of the energy peak slightly decreases as $\alpha$ increases, being equal to $S_t \approx 0.089$ at $\alpha = 8°$. This effect is probably connected to the variation of the incoming boundary layer properties as the incidence increases.



(i) Results for sensor **a**.

(ii) Results for sensor **b**.
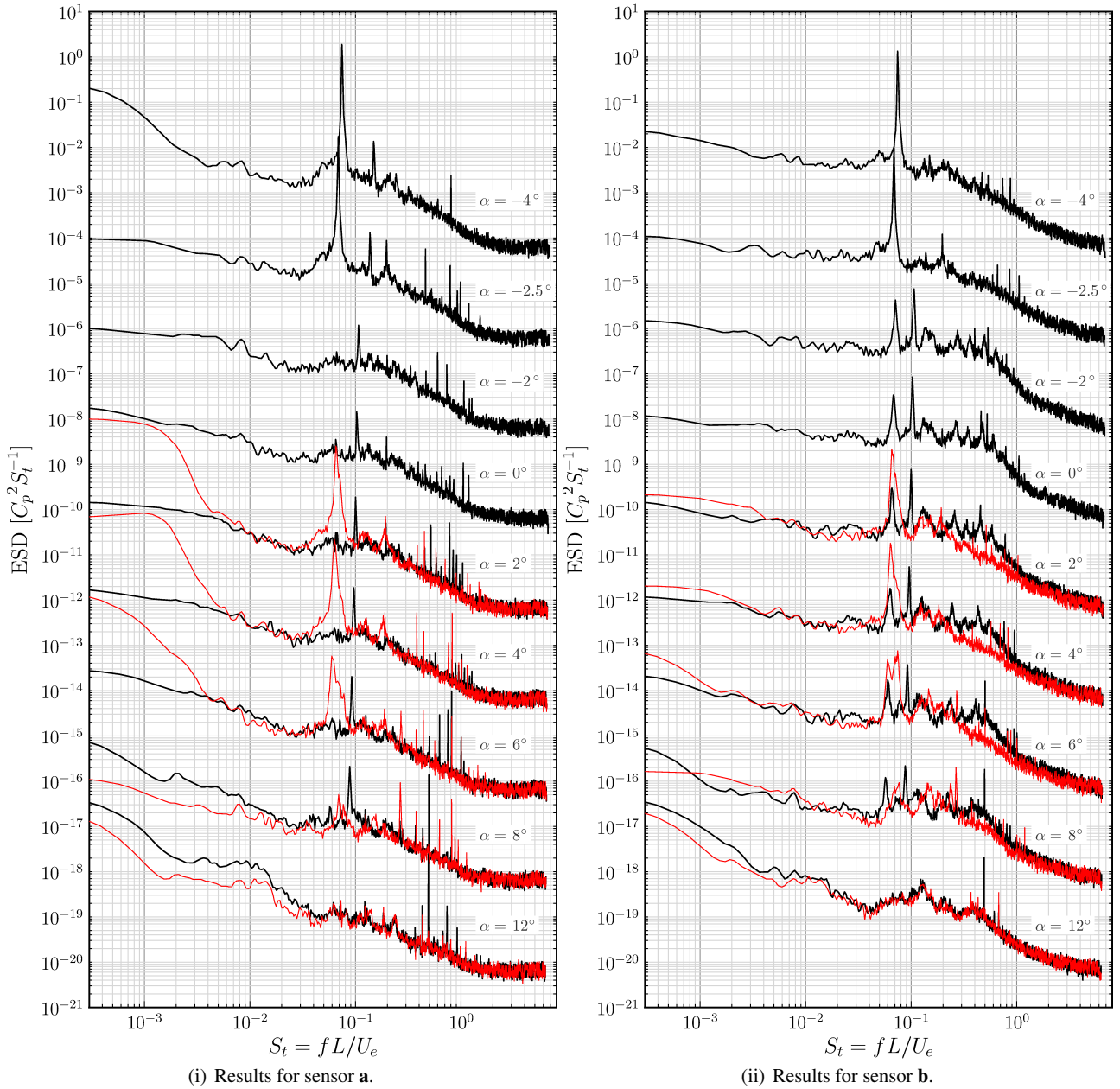
**Fig. 13** Pressure coefficient energy spectra for angles of attack $-4° \leqslant \alpha \leqslant 12°$. TVCS configuration, $S = 0.0037$, $Re = 10^6$. For clarity, after the first spectrum, $\alpha = 4°$, each curve is translated downwards by two decades. The red, thinner lines refers to the HD cases.

For $\alpha \geqslant 2°$ the spectra for both modes were reported, (LD black, HD red curves). The spectra evidence a further cavity flow transition for $\alpha = 2°$. In fact, at this incidence the spectrum of the HD mode shows a peak of energy concentration roughly at the same Strouhal number of $\alpha = -4°$ and $-2.5°$. In the range $2° \leqslant \alpha \leqslant 6°$, the spectra associated with the HD mode present a broadband low frequency component for $S_t \lesssim 2 \cdot 10^{-3}$. In the knowledge of the authors, there are no literature results for cavity flows which report a similar low frequency component but a possible explanation is given later in the paper.

More insight into the transitions occurring at $\alpha = -2.5°$ and $\alpha = 2°$ is given by the spectra of sensor **b**, figure 13(ii), located at the downstream edge of the cavity. As before, for $\alpha \geqslant 2°$, the spectra for both the LD and HD modes have been reported. For $\alpha = -4°, -2.5°$ and for $2° \leqslant \alpha \leqslant 8°$, for the HD mode, the same peak observed in location **a** is observed in **b**. This peak, associated to the wake mode, confirms that the intense fluctuations are due to a large scale structure which influences both **a** and **b** and probably the whole cavity, as reported by Rowley et al (2001) and Suponistsky et al (2005). Instead, for the spectra corresponding to the LD mode, for $-2° \leqslant \alpha \leqslant 6°$, a high energy concentration is present in the range $0.2 < S_t < 0.9$, and several other weak peaks can be observed. These Strouhal numbers are typically observed for the shear layer oscillation mode for cavity flows. This behaviour is driven by a feedback process in which small disturbances develop in the shear layer, spanning the cavity and separating from the cusp, via a Kelvin-Helmholtz instability. The interaction between the disturbances and the downstream cavity's edge is propagated upstream towards the cusp, influencing the separating shear layer. For Mach numbers approaching zero, the literature, Rowley et al (2001); Suponistsky et al (2005), reports for rectangular cavities values of the Strouhal number based on the cavity length in the range $0.5 < S_{t_L} < 1$. Furthermore, in this flow regime a stable primary vortical structure occupies the rectangular cavity, as shown by Rowley et al (2001) and Faure et al (2009), which interacts weakly with the shear layer. A stable vortex has been observed trapped inside cavities with a geometry similar to that used in the present experiment by several authors, for example by Savelsberg and Castro (2008); Hokpunna and Manhart (2007); De Gregorio and Fraioli (2008).

For the LD mode the spectra of sensors **b** present a weak peak at $S_t \approx 0.075$, probably still associated to the wake mode, and a second peak at $S_t \approx 0.11$.

For the higher incidences, $\alpha = 8°$ and especially $\alpha = 12°$, the spectra do not show strong energy peaks. Probably a different flow regime takes place, as a consequence of the interaction of the cavity flow with the downstream separation region.

It is argued that the observed flow reorganizations at specific angles of attack and for a given suction rate may be
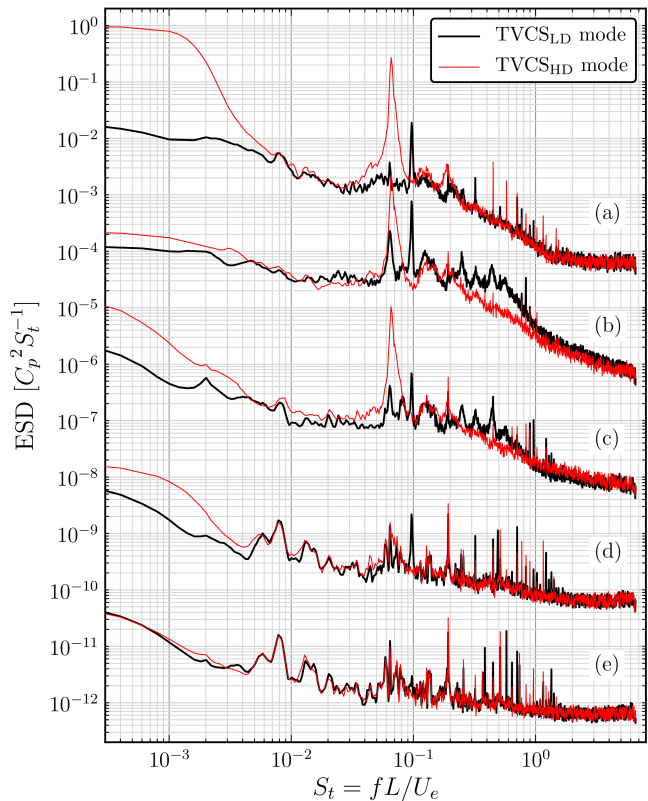


**Fig. 14** Energy spectra for the LD, (black, thick lines), and HD case, (red, thinner lines). $\alpha = 2°$, $S = 0.0037$, $Re = 10^6$. See figure 1 for the sensors' position.

related to the variation of the properties of the boundary layer approaching the cavity as the incidence is varied. In fact, as shown by several authors for rectangular cavity flows, Gharib and Roshko (1987); Rowley et al (2005), at specific values of the cavity length to boundary layer momentum thickness ratio $L/\theta$, a flow transition is triggered. Similar transitions in the spectral characteristics were also observed by Olsman and Colonius (2011) for the flow in a cavity positioned over an airfoil, when the angle of attack was changed.

Analogous transitions in the spectral characteristics of the pressure fluctuations were observed when varying the suction rate at a fixed angle of attack. These transitions occured for the critical suction rates evidenced in figure 12, for which the drag coefficient was suddenly reduced. Before the transition, the spectra of the cavity sensors' fluctuations were characteristic of the HD mode, while after the transition the spectra were similar to those of the LD mode.

In figure 14, the spectra related to the five sensors and for both drag modes are presented for $\alpha = 2°$, where the drag coefficient curve of the TVCS configuration bifurcates. For the HD mode, all the sensors inside the cavity, (**a**, **b** and **c**), are probably strongly subjected to the effects of the wake mode, as suggested by the peak located at $S_t \approx 0.065$. A weak peak at the same Strouhal number also appears for the LD mode, for the sensors in the cavity. On the other

hand, for the LD mode, only transducers **b** and **c** present high energy in the range $0.2 < S_t < 0.9$, associated to the shear-layer mode, since they are located near the shear layer impingement region. Notice that the spectrum shows a high energy content at low frequencies only for sensor **a** and only for the HD mode.

Furthermore, for both modes the spectra of locations **a**, **b** and **c** are significantly different from those located outside the cavity. The first three sensors are in fact affected by the cavity flow, while sensors **d** and **e** are more influenced by the wall-bounded flow developing downstream of the cavity. Nevertheless, for the HD mode a very weak peak of energy centred at the same Strouhal number associated with the wake mode is observed for these two sensors. This could be attributed to the action of the flow structures advected downstream on the external part of the boundary layer, which periodically perturb the wall flow.

The spectra for the TVCS configuration at $Re = 6.67 \cdot 10^6$, not reported here for brevity, have very similar characteristics to those reported in figure 14 for the HD mode, since all the sensors in the cavity show a strong peak at a reduced frequency of the order of 0.07, corresponding to the wake mode. No evidence of a shear layer mode was found at the lower Reynolds number. This result seems to justify the fact that the drag of the TVCS configuration was always higher than that of the classical boundary layer suction configuration at the lower Reynolds number.

As discussed for figure 13(i) and figure 14 for location **a**, a high energy low frequency component characterizes the spectra of the HD mode for $2° \leqslant \alpha \leqslant 6°$. In figure 15(a) the time history of the pressure fluctuation for sensor **a** at $\alpha = 2°$ is reported, covering about 10% of the whole time history. The smooth dark line is the low pass filtered time history, shown to clearly highlight the contribution of the lower frequency component. The abscissa is the non dimensional time $tU_e/L$, where $U_e$ and $L$ are the external speed computed from the static pressure distributions and the cavity opening length, respectively. Figure 15(b) shows the corresponding spectrogram of the pressure time history. The spectrogram was computed by means of a Short-Time-Fourier-Transform with 50% overlapping blocks of $2^{11}$ points, which correspond to approximately 160 non dimensional time units, giving a frequency resolution of $\Delta S_t \approx 0.00635$. The blocks were tapered with a Hanning window. Finally, figure 15(c) shows the time evolution of the energy spectral density for $S_t = 0.0635$. The pressure signal is characterized by large scale variations of the local mean value, as high as $\Delta C_p \approx 0.1$. Such modulation is responsible for the low frequency component observed in the spectra. Interestingly, the pressure modulation is associated to strong variations of the energy distribution: when the mean pressure coefficient rises, the energy content of the signal at $S_t \approx 0.0635$ decreases drastically by several orders of magnitude, (figures 15(b) and 15(c)).

Similar characteristics were observed for sensor **b** located on the downstream cavity edge, as shown in figure 16. In this case, however, no large scale pressure coefficient variations are observed even though strong energy redistributions occasionally take place. In particular, when the energy at $St = 0.063$, corresponding to the wake mode, decreases, high energy is observed at higher frequencies, which correspond to the shear layer mode.

This intermittency of the energy characteristics of the pressure signal may be interpreted as the result of an intermittent switch of the cavity flow regime. Similar intermittent flow reorganizations have also been pointed out by the numerical simulations of Rowley et al (2001). For certain threshold values of the ratio $L/\theta$, (cavity length to incoming boundary layer momentum thickness), the authors observed the presence of switching between the shear layer mode and the wake mode. Analogously, it is possible that in our experiment the observed intermittency was caused by the values of $S$ and $\alpha$ being close to critical values.

An intermittent behaviour of the energy content, but with different characteristics, was also observed in the signal of the LD mode. In figure 17 results for the LD mode at $\alpha = 2°$, $S = 0.0037$ and for sensor **b** are reported. The energy intermittency takes place over a much shorter time scale and involves several frequencies. Furthermore, high energy is intermittently observed at $St = 0.063$, associated to the wake mode. This result can be attributed to the fact that, even for the LD case, the wake mode was occasionally triggered.

The frequency of some of the observed peaks is close to the first acoustical transversal resonance of the test section, which at $Re = 10^6$ is equal to $St = 0.11$, approximating the test section as rectangular, AGARD-AR-336 (1998). However, if this were the case the same spectral component should have emerged for all sensors, for all the drag cases and for all the incidences. As discussed, this was not observed in the experiments, so the possibility of a resonance condition should be excluded.

### 3.4.2 Auto-correlation functions

Auto-correlation coefficient functions of the pressure fluctuations for the five sensors are reported in figure 18 for $\alpha = 2°$, at $Re = 10^6$ and for both drag modes. The results at this incidence are very similar to those of $\alpha = 4°$ and $\alpha = 6°$, and are representative of the behaviours of the HD and LD modes. The auto-correlation function is defined as:

$$\rho_{ii}(\tau) = \frac{\overline{p'_i(t)p'_i(t+\tau)}}{\overline{p'_i(t)^2}} \tag{1}$$

where $p'_i(t)$ is the pressure fluctuation of the generic sensor $i$, $\tau$ is the time lag and the "overline" denotes a time average.

It is observed that for the HD mode the pressure fluctuations at locations **a**, **b** and **c** (cavity sensors) give a slow decay
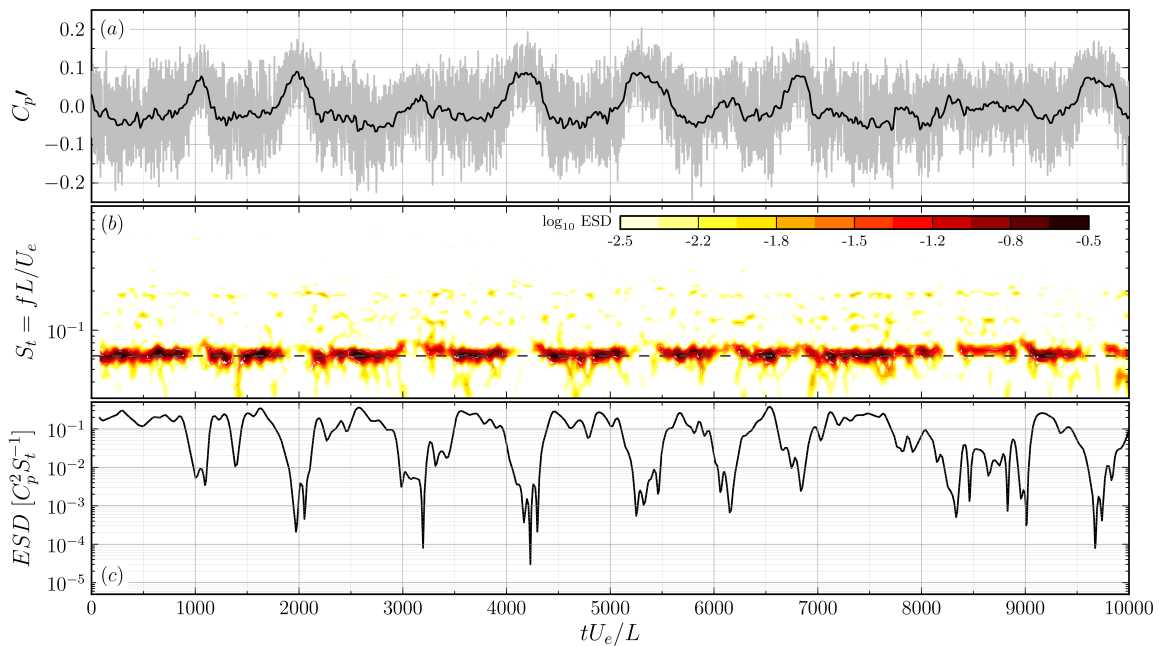
**Fig. 15** Pressure signal characteristics for sensor **a** at $\alpha = 2°$, HD case, $S = 0.0037$. Fluctuating pressure coefficient time history and low pass filtered signal, (dark line) (a); spectrogram of the pressure signal, (b); time dependent energy content of the signal at $S_t = 0.063$, (c).
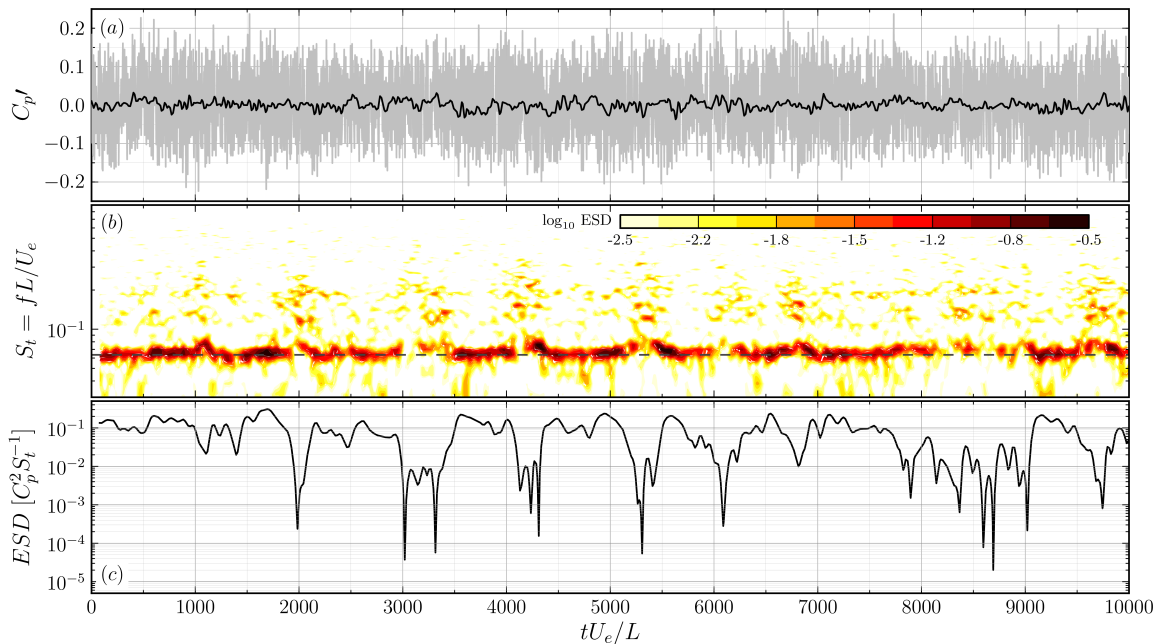


**Fig. 16** Pressure signal characteristics for sensor **b** at $\alpha = 2°$, HD case, $S = 0.0037$. Fluctuating pressure coefficient time history and low pass filtered signal, (dark line) (a); spectrogram of the pressure signal, (b); time dependent energy content of the signal at $S_t = 0.063$, (c).
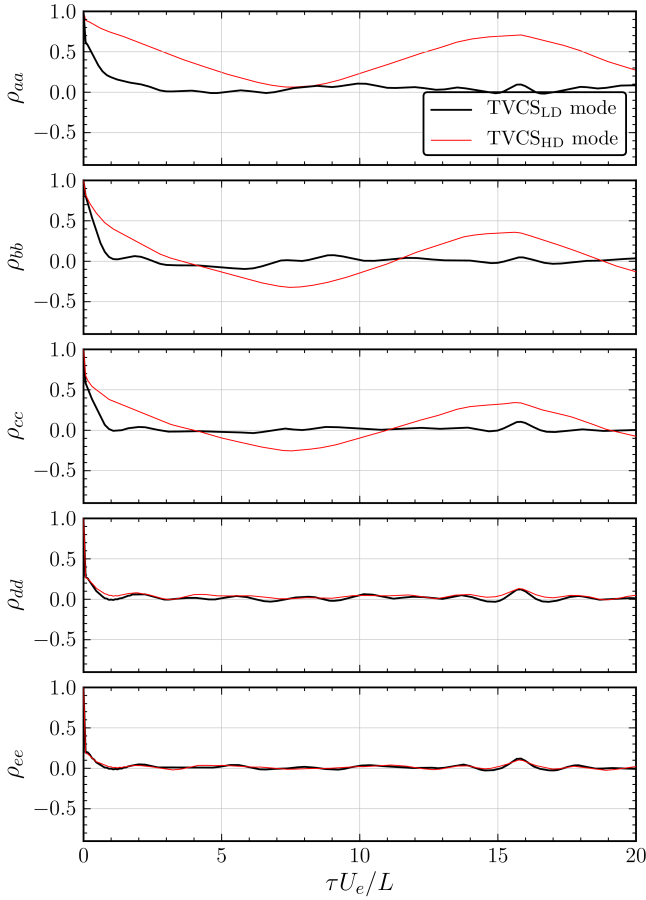
of the auto-correlation functions, which show a periodicity with a non dimensional period $\tau U_e/L = 15.8$, which is approximately the reduced frequency equal to 0.065 appearing in the spectra. This could be interpreted as the footprint of the large scale structures of the wake mode forming in the cavity. This was proved by computing the autocorrelation functions of the filtered signals: when the component at $S_t = 0.065$ was filtered out, the signals decorrelated much more quickly.

On the other hand, in the same locations, the auto-correlation functions corresponding to the LD mode quickly decay to zero. Such a result is interpreted by the authors as due to the boundary layer flow on the cavity's wall, generated by a well organized trapped vortex, as was evidenced by De Gregorio and Fraioli (2008) for a configuration similar to that of the present experiment. In a boundary layer flow, the autocorrelation of the pressure signal typically decays quickly.
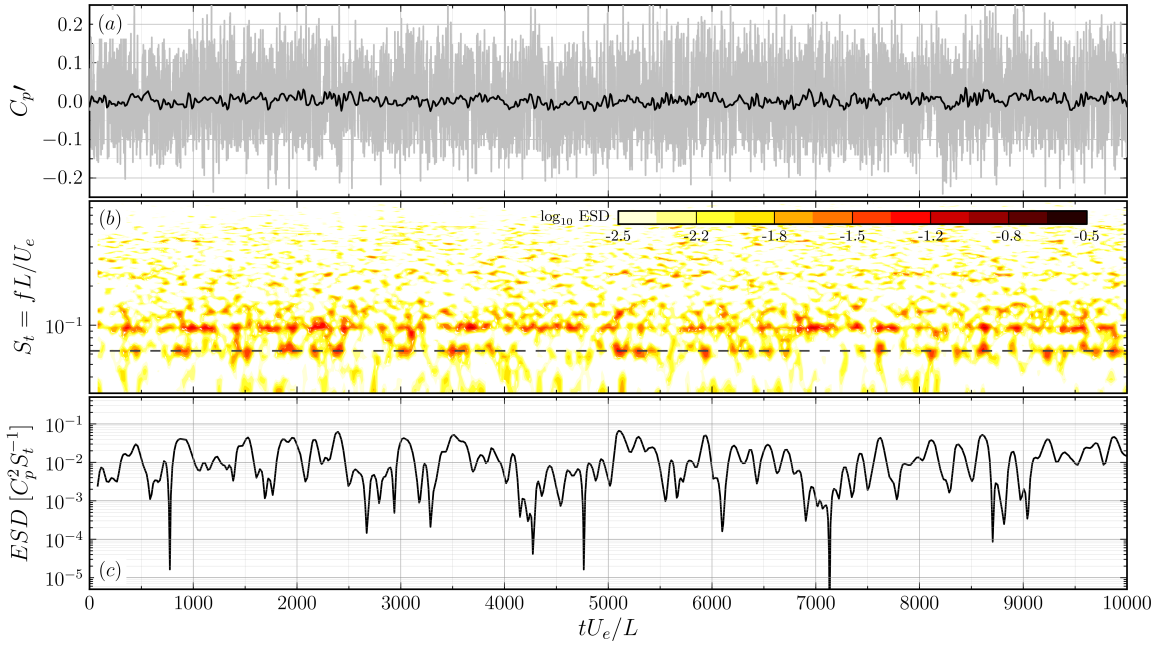
**Fig. 17** Pressure signal characteristics for sensor **b** at $\alpha = 2°$, LD case, $S = 0.0037$. Fluctuating pressure coefficient time history and low pass filtered signal, (dark line) (a); spectrogram of the pressure signal, (b); time dependent energy content of the signal at $S_t = 0.063$, (c).



**Fig. 18** Auto-correlation functions of the fluctuating pressure time histories for the LD and HD modes. $\alpha = 2°$, $S = 0.0037$, $Re = 10^6$.

For the sensors located outside the cavity, the auto-correlation functions show a rapid decay, with a similar behaviour for both drag modes. Again this is probably due to the fact that these two sensors are subjected to the effect of the wall bounded flow developing downstream of the cavity.
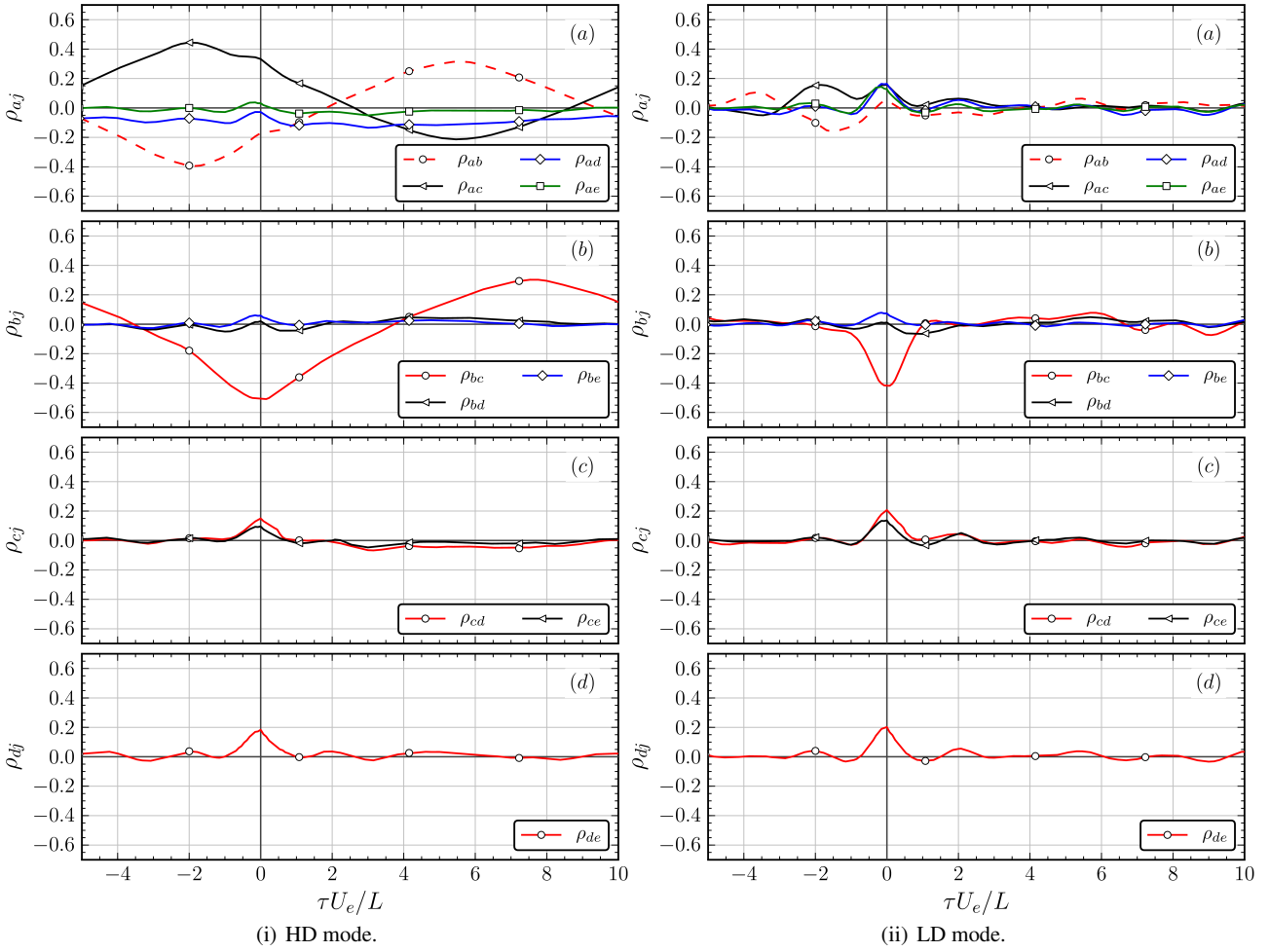
### 3.4.3 Cross-correlation functions

Cross-correlation coefficient functions of the pressure fluctuations between two different generic locations $i$, $j$ are shown in figures 19(i) and 19(ii), for $\alpha = 2°$, and for the LD and HD mode, respectively. These results show the cross-correlation functions between sensor $i$ and the remaining downstream sensors $j$. The cross-correlation coefficient function is defined as:

$$\rho_{ij}(\tau) = \frac{\overline{p_i'(t)p_j'(t+\tau)}}{\overline{p_i(t)'^2}^{1/2} \cdot \overline{p_j(t)'^2}^{1/2}} \quad (2)$$

Considering the results related to the HD mode and for sensor **a**, figure 19(i)-a, it is visible that the signal is highly correlated with those at location **b** and **c**, with a peak correlation value equal to -0.4 and 0.5 respectively, obtained at $\tau U_e/L = -2$. This negative time lag means that the pressure disturbance responsible for the high correlation is first observed in **b** and **c** and then in **a**. Furthermore, the pressure signals at locations **b** and **c** are negatively well correlated, with a zero time lag, because of the proximity of these two sensors.

The fact that the pressure fluctuations measured by sensors **a**, **b** and **c** are well correlated between each other may be

**Fig. 19** Cross-correlation functions of the pressure fluctuations for the five sensors. $\alpha = 2°$, $S = 0.0037$, $Re = 10^6$. One out of 40 data points is shown, for clarity.

further evidence of the wake mode. In fact the large scale motions associated to this oscillation mode are of the same size as the cavity and therefore they could influence the whole cavity region. In fact, by evaluating the cross-correlation functions of the filtered signals it was proved that the high level of cross-correlation is mainly due to the frequency component centred at $S_t \approx 0.065$, associated with the wake mode.

It is interesting to observe that the effects of this perturbation are bounded within the cavity because of the poor correlation between the signals of the sensors in the cavity, **a**, **b** and **c**, with those of the sensors located outside, **d**, **e**.

Regarding the LD case, figure 19(ii), the most important feature is a generally lower correlation between the sensors in the cavity, compared to the HD case. As discussed above, in the LD mode the cavity may be filled with a well organized vortical structure, which generates a boundary layer flow over the cavity's wall. In this situation the pressure fluctuations at two separate locations should be strongly decorrelated.

An exception to the general low cross-correlation for the LD case is represented by sensors **b** and **c** for which

$\rho_{b,c}(0) \approx -0.4$, not dissimilar to the corresponding value of the HD case. This might be connected to the proximity of the two sensors to the stagnation region, where the separated shear-layer impinges, influencing both sensors.

For both modes there is some degree of correlation between locations **a**, **b** and **c** and sensors **d** and **e**. These weak correlation peaks, all centred at $\tau U_e/L = 0$, are probably generated by the high frequency noise evidenced in the spectra of figures 13 and 14.

## 4 Discussion and conclusions

The effectiveness of a trapped vortex cell in controlling the the flow past a thick wing profile was tested experimentally at $Re = 10^6$ and $6.67 \cdot 10^5$. The cavity flow was controlled by suction, operated over its upstream part. A comparison with a classical boundary layer suction configuration was also performed.

Complex behaviour of the drag curve was observed for the TVCS configuration, at the higher Reynolds number and for the maximum suction rate. In fact, the drag curve presented two branches, separating at $\alpha = 2°$ and converging at $\alpha = 12°$, giving a low drag and a high drag mode.

Compared to the conventional boundary layer suction system, (BS configuration), the TVCS control gave larger drag reductions for the same amount of suction only in the range $-2° \leqslant \alpha \leqslant 8°$ and only if the low drag mode was considered. Outside this incidence range, and especially at high angles of attack, the classical boundary layer suction system appeared to be more effective. Furthermore, these benefits were observed only for the higher Reynolds number, while for $Re = 6.67 \cdot 10^5$ the conventional boundary layer suction system always gave a lower drag coefficient.

In terms of lift, the BS configuration gave slightly higher benefits in the stall region with respect to the TVCS configuration. At low/mid incidences the lift increments of the TVCS and BS configurations were practically equal.

The two drag branches of the TVCS configuration were associated to two different cavity flow regimes. In fact, complex, intermittent behaviour emerged from the spectral analysis of the fluctuating pressure signals. The high drag mode was associated to the wake mode, usually described in terms of a large scale vortex shedding from the cavity. This was evidenced by a strong energy peak at a Strouhal number equal to 0.065, by large integral time scales and by high cross-correlation values of the pressure fluctuations inside the cavity. On the other hand, the LD mode was associated to a flow regime corresponding to a stable and well organized vortical structure trapped inside the cavity. In this condition a shear layer mode takes place, evidenced by the spectral analysis of the sensors in the shear layer impingement region as high energies in the range $0.2 < St < 0.9$. Further evidence of such a regime were the low integral time scale and low cross-correlation for the sensors inside the cavity, as a result of the boundary layer developing on the cavity's wall.

Transitions between the two modes were also observed when varying the suction rate at a fixed angle of attack. In fact, at specific critical values of the suction rate, the drag coefficient was drastically reduced.

A very complex flow originates in the cavity region due to the interaction of the cavity flow, the shear layer separating from the cusp and the external flow. Such a acomplex interaction is strongly influenced by some important flow parameters, namely the angle of attack, the Reynolds number and in particular the suction rate. However, a clear description of the underlying mechanisms and of the role of these parameters remains open to discussion and to further investigation. However, the effectiveness and the robustness of the TVC flow control technique critically depend on the understanding and of the control of these mechanisms.

The flow in the cell showed a three-dimensional organization in the spanwise direction, according to the value of the suction and of the incidence. More interestingly, a three-dimensional spanwise organization was found for both drag modes, leading to the conclusion that these three-dimensional effects are probably not so important for the effectiveness of the TVC control technique.

Regarding the drag reduction of the TVCS configuration with respect to the classical boundary layer suction system, it is argued that the coherent and stable vortex trapped inside the cavity in the LD mode could originate a "wall-slip layer" effect. In this condition, the presence of a tangential velocity at the interface with the external flow produces higher momentum in the near wall region downstream of the cavity, with respect to the classical boundary layer suction system, resulting in a more filled boundary layer. As a consequence this would be characterized by a lower momentum thickness up to the trailing edge, resulting in a narrower wake, that is a lower drag. On the other hand, in the HD flow regime, since no steady vortex is present in the cell, the drag reduction associated with the "wall-slip layer" effects is lost and the drag reduction with respect to the baseline case is probably connected to the effects of the suction inside the cavity.

# References

Adkins R (1975) A short diffuser with low pressure loss. J Fluids Eng 97:297–302

AGARD-AR-304 (1994) Quality assessment for wind tunnel testing. NATO Research and Technology Organisation

AGARD-AR-336 (1998) Wind tunnel wall corrections. NATO Research and Technology Organisation

Brès A G, Colonius T (2008) Three-dimensional instabilities in compressible flow over open cavities. J Fluid Mech 599:309–339

Chernyshenko SI, Castro IP, Hetsch T, Iollo A, Minisci E, Savelsberg R (2008) Vortex cell shape optimization for separation control. In: 5th. European Congress on Computational Methods in Applied Sciences and Engineering (ECCOMAS 2008), Venice, Italy

Choi KS, Fujisawa N (1993) Possibility of drag reduction using d-type roughness. Appl Sci Res 50:315–324

De Gregorio F, Fraioli G (2008) Flow control on a high thickness airfoil by a trapped vortex cavity. In: 14th International Symposium on Applications of Laser Techniques to Fluid Mechanics, Lisbon, Portugal

Donelli R, Chernyshenko S, Iannelli P, Iollo A, Zannetti L (2009) Flow models for a vortex cell. AIAA Paper 2(47):451–467

Faure T, Pastur L, Lusseyran F, Fraigneau Y, Bisch D (2009) Three-dimensional centrifugal instabilities development inside a parallelepipedic open cavity of various shape. Exp Fluids 47(3):395–410

Gharib M, Roshko A (1987) The effect of flow oscillations on cavity drag. J Fluid Mech 177(1):501–530

Hokpunna A, Manhart M (2007) A large-eddy simulation of vortex cell flow with incoming turbulent boundary layer. Int J Mech Syst Sci Eng 1:123–128

Hung L, Moin P, Kim J (1997) Direct numerical simulation of turbulent flow over a backward-facing step. J Fluid Mech 330:349–374

Iollo A, Zannetti L (2001) Trapped vortex optimal control by suction and blowing at the wall. Eur J Mech B-Fluid 20(1):7 – 24

Kasper W (1974) Aircraft wing with vortex generation. U.S Patent No.3831885

Larchevêque L, Sagaut P, Labbé O (2007) Large-eddy simulation of a subsonic cavity flow including asymmetric three-dimensional effects. J Fluid Mech 577:105–126

Maull D, East L (1963) Three-dimensional flow in cavities. J Fluid Mech 16:620–632

Migeon C (2002) Details on the start-up development of the Taylor-Gortler-like vortices inside a square-section lid-driven cavity for $1,000 <$Re$< 3,200$. Exp Fluids 33:594–602

Olsman WFJ, Colonius T (2011) Numerical simulation of flow over an airfoil with a cavity. AIAA Journal 49:143–149

Ringleb F (1961) Separation control by trapped vortices. In: Boundary Layer and flow control, Pergamon Press, Ed. Lachmann G.V.

Rockwell D, Knisely C (1980) Observations of the three-dimensional nature of unstable flow past a cavity. Phys Fluids 23:425–431

Rockwell D, Naudascher E (1979) Self-sustained oscillations of impinging free shear layers. Annu Rev Fluid Mech (11):67–94

Rossiter J (1964) Wind-tunnel experiments on the flow over rectangular cavities at subsonic and transonic speeds. Aero Res Counc (No. 3438)

Rowley C, Colonius T, Basu A (2001) On self-sustained oscillations in two dimensional compressible flow over rectangular cavities. J Fluid Mech 455:315–345

Rowley C, Juttijudata V, Williams D (2005) Cavity flow control simulations and experiments. AIAA Paper 292:1–11

Savelsberg R, Castro I (2008) Vortex flows in open cylindrical-section cavities. Exp Fluids 46(3):485–497

Savitsky A, Schukin L, Kareljn V (1995) Method for control of the boundary layer on the aerodynamic surface of an aircraft, and the aircraft provided with boundary layer control system. U.S Patent No. 5417391

Schlichting H (1954) Boundary layer theory, 1st edn. Springer

Suponistsky V, Avital E, Gaster M (2005) On three dimensionality and control of incompressible cavity flow. Phys Fluids 17(104103)